

Level-set based pre-processing algorithm for particle-based methods

Yongchuan Yu^a, Yujie Zhu^{b,c}, Chi Zhang^b, Oskar J. Haidn^a, Xiangyu Hu^{b,*}

^a*Chair of Space Propulsion and Mobility, Technical University of Munich, 85521 Ottobrunn, Germany*

^b*Chair of Aerodynamics and Fluid Mechanics, Technical University of Munich, 85748 Garching, Germany*

^c*Xi'an Research Institute of High-Tech, 710025 Xi'an, China*

Abstract

Obtaining high quality particle distribution representing clean geometry in pre-processing is essential for the simulation accuracy of the particle-based methods. In this paper, several level-set based techniques for cleaning up ‘dirty’ geometries automatically and generating homogeneous particle distributions are presented. First, a non-resolved structure identifying method based on level-set field is employed to detect the tiny fragments which make the geometry ‘dirty’ under a given resolutions. Second, a re-distance algorithm is proposed to remove the tiny fragments and reconstruct clean and smooth geometries. Third, a ‘static confinement’ boundary condition is developed in the particle relaxation process. By complementing the kernel support for the particles near the geometric surface, the boundary condition achieves better body-fitted particle distribution on the narrow region with high curvature. Several numerical examples include a 2D airfoil 30P30N, 3D SPHinXsys symbol, a skyscraper with a flagpole and an inferior vena cava demonstrate that the present method not only cleans up the ‘dirty’ geometries efficiently, but also provides better body-fitted homogeneous particle distribution for complex geometry.

Keywords: Particle methods, ‘dirty’ geometry cleaning, level-set, static confinement, kernel support completing

1. Introduction

As a truly Lagrangian, mesh-free method, smoothed particle hydrodynamics (SPH) has attracted tremendous attention due to its very nature of tracking moving characteristics such as free surfaces, moving and deformable material

*Corresponding author.

Email addresses: yongchuan.yu@tum.de (Yongchuan Yu), yujie.zhu@tum.de (Yujie Zhu), c.zhang@tum.de (Chi Zhang), oskar.haidn@tum.de (Oskar J. Haidn), xiangyu.hu@tum.de (Xiangyu Hu)

interfaces. Typical applications include geophysical flow [1, 2, 3], bio-mechanics [4, 5, 6, 7] and other industrial application [8, 9, 10]. Specifically, the SPH method has been successfully implemented in the modeling of bird impact [11, 12], aircraft ditching [13], wave energy conversion process [14], ocean and coastal engineering [15, 16, 17], high-velocity impact welding [18], and slurry & media motion within stirred media detritor (SMD) [19], to name a few.

To eliminate the bottleneck for widespread industrial applications of SPH method, one critical challenging task in pre-processing is to efficiently generate body-fitted and isotropic particle distribution for arbitrarily complex geometry. In many applications of the SPH method, the lattice-based and volumetric-mesh converted particle distributions [20, 21] are still the most popular approaches [10]. While the former is not body-fitted for complex geometry, the latter is difficult to be isotropic. When SPH particles are used to model a fluid in the Lagrangian framework, it seems that the initial particle distribution does not need to be body-fitted or isotropic as, after the simulation starts, the particles always leave their initial position and form isotropic distribution due to the self-adjust mechanism. Even this, since the particles are not initially set in the ‘equilibrium’ position, the numerical noise introduced by particle resettlement during the early stages of the flow evolution will strongly affect the fluid evolution [22]. Furthermore, as the development of more challenging SPH algorithms and complex applications in the field of bio-medicine[4], structural mechanics[23], fluid-structure interaction [24, 25, 26], and SPH method in Eulerian framework [27, 28], in which the particle configuration is fixed through the simulation, generating body-fitted and isotropic particle distribution for general complex geometries are becoming more significant.

In order to achieve this goal, several different approaches have been proposed. Particle packing algorithm [22] provide a ‘equilibrium’ initial distribution of fluid particles with simple geometries where solid particles are prescribed for the surface. The weighted Voronoi tessellation (WVT) algorithm [29] iterates the particle distance under a repulsive force to achieve a quasi-isotropic uniform or non-uniform particle distribution for arbitrary geometry. This method needs to exert anti-symmetric forces from the ghost particles to prevent the penetration. The Extended WVT algorithm [30, 31, 12] represents the geometry surface by shell mesh elements in order to treat more complex boundaries. By introducing level-set to describe the geometry while solving the target feature-size function, Fu et al. [32] proposed a fluid relaxation method, which is able to generate isotropic and body-fitted particle distribution for arbitrary 2D geometry. Ji et al. [33, 34] extended the fluid relaxation method with a feature boundary correction term to accelerate the particle generation process and to address the issue of incomplete kernel support near the surface. By replacing the governing equation with an original momentum equation in particle discrete form, Zhu et al.[35] further simplified the relaxation method to a physics-driven relaxation process with a simple level-set based bounding method.

While the relaxation-based methods are able to generate body-fitted and isotropic particle distributions, when the local length scale or curvature of the geometry does not variate too much (except singularities), they face a critical

issue, similar to the mesh-based method [36], when the local length scales of the body surface span a large range. One typical case is the problem of ‘dirty’ geometry, which frequently occurs in industrial simulations and brings lots of extra manual labor, but has been rarely discussed in the literature. ‘Dirty’ geometries involve small structures or small flow paths with the characterized size which can not be well resolved in the simulations [37], and often induce low-quality mesh or particle distribution and eventually to numerical instability. Besides erasing these small structures manually, another straightforward approach is capturing such small features directly, which may increase the total number of grid points or particles dramatically and leads to extremely small time-step sizes [37]. One alternative way to circumvent this issue for the mesh-based method is introduced an effective smearing technique by which the influence of small structures is smeared out with the immersed boundary method (IBM) [37]. While this technique shows good performance in many cases, the overlap meshes and heterogeneous coupling used in IBM are not always desirable, especially when conservation properties are required. To the best knowledge of the authors, the proper approach for handling the ‘dirty’ geometry problem is yet to be proposed for particle methods.

Another issue of the particle relaxation method is the boundary condition for body-fitting. As the particle relaxation takes place inside the geometry, and there are no particles outside the surface to achieve force balance or full kernel support, a boundary condition should be imposed for the particles near the surface. A typical approach for this is the ghost particle method, in which ghost particles are used to fill the outside space near the surface [38, 39, 40, 32]. While introducing ghost particles for simple surfaces is straightforward, it can be quite a challenge for complex geometry. In addition, more particles also lead to additional computational and memory cost, especially for three-dimensional problems. Ji et al. [34] exploited a ‘feature boundary correction’ term to mimic the fully kernel support for the boundary particles near the surface. This method still requires a single layer of particles generated on the surface, which is not trivial for complex three-dimensional geometries, and relaxing together with the interior particles. Zhu et al. [35] introduced a simple and fast particle bounding method without using ghost or surface particles. The bounding method directly constrains the boundary particles according to their distances toward the surface probed from the background level-set field. While being quite effective when the surface curvature is moderate, it does not converge, typically presented by particles with persistent and fast motion, to the balanced particle distribution near sharp features of the surface.

In this paper, a level-set based pre-processing techniques for particle-based applications are proposed to solve the above-mentioned problems. First, a non-resolved structure identifying method based on level-set field is employed to find out those tiny fragments which make the geometry becomes ‘dirty’ under a given resolution. Second, a re-distance method is used to reconstruct the level-set field by removing these ‘dirty’ geometries. The particle generation process for the 30P30N airfoil is employed to show the instability caused by ‘dirty’ geometry in particle relaxation. This example also demonstrates that our method generates

the isotropic body-fitted particle distribution for arbitrary complex geometries by identifying and cleaning-up the non-resolvable small structures. At last, a new level-set based method named ‘static confinement’ is developed to complete the kernel function on the geometry surface during the physics-driven relaxation process. With the ‘static confinement’ boundary condition, the geometries with large curvature corners can be accurately captured.

The remainder of this paper is organized as follows. In Section 2, we briefly summarize the previous particle-relaxation method for body-fitted particle generation and the narrow-band level-set technique. In Section 3, the algorithm for identifying and cleaning-up the non-resolvable small structures are presented. The method of ‘static confinement’ is developed in Section 4 to complete the SPH kernel support during the particle relaxation process. Several typical applications are shown in Section 5 to validate the importance of the ‘dirty’ geometry cleaning-up process and the self-cleaning ability of the present pre-processing tool, respectively. Concluding remarks are given in Section 6. The source code of the present method is available in our open-source SPHinXsys library [41, 42] at <https://www.sphinxsys.org>.

2. Preliminary work

In this section, we briefly summarize the particle-relaxation method on generating body-fitted particle distributions for arbitrarily complex geometries and more details are referred to Ref. [35].

2.1. level-set method and narrow-band technique

To represent the complex geometry, the level-set field $\phi(x, y, z, t)$ is utilized by defining a signed distance function, so that the zero level-set contour

$$\Gamma = \{(x, y, z) | \phi(x, y, z, t) = 0\}. \quad (1)$$

represents the geometry surface, and the negative and positive level-set values are for the inside and outside regions respectively. The normal direction $\mathbf{N} = (n_x, n_y, n_z)^T$ can be evaluated by

$$\mathbf{N} = \frac{\nabla\phi}{|\nabla\phi|}. \quad (2)$$

To discretize the level-set field, a Cartesian background mesh is used in the whole computational domain and the level-set value ϕ of each mesh cell is defined by the distance from the cell center to the geometry surface. Subsequently, the level-set field can be constructed by parsing CAD data with proper in-house function or parser provided by open source library, for example Simbody [43] and Boost libraries.

A typical way to reduce the computational effort for level-set related operations is the narrow-band method [44, 45, 46], in which the computation effort

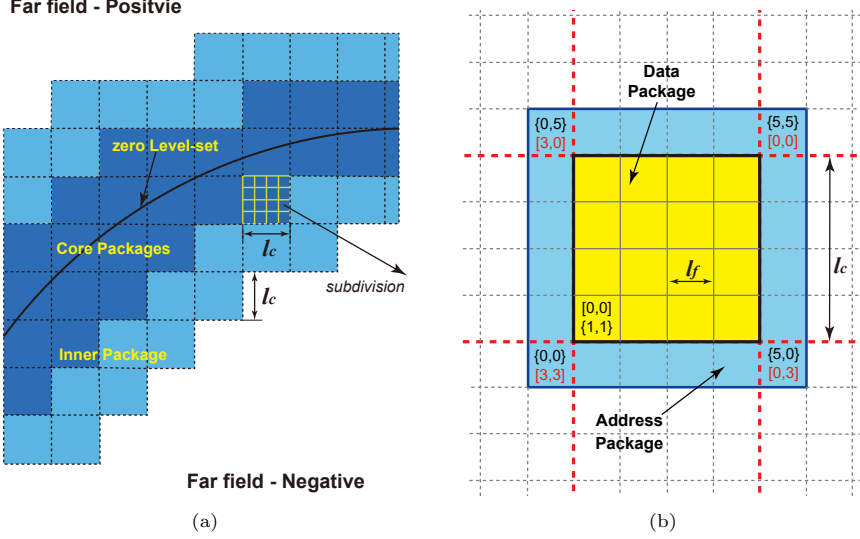


Figure 1: level-set field with narrow band data storage: (a) ‘inner packages’(light blue cells) and ‘core packages’(dark blue cells) around geometry surface, (b) structure of data-package (yellow cells) and address-package (blue cells). The square brackets indicate a data sequence in the ‘data package’. The curly brackets indicate the address sequence in the ‘address package’. All the black indexes are belong to the same ‘data package’ and its ‘address package’, while the red indexes are from its neighbor ‘data package’.

is restricted to the near-interface band. Here, the narrow-band technique similar to Refs. [45, 47] is used with memory-pool data package technique [47] for further accelerating the level-set related operations.

Fig. 1 gives a detailed description of the narrow-band and data package settings. Here, the narrow-band region near the geometry surface is further divided into the core region and the inner region (the inner region contains the core region) represented by mesh cells with a coarse cell spacing l_c . Each mesh cell in the narrow-band region has been subdivided into 4×4 (in 2D) data grids with the fine cell spacing l_f equals to a quarter of l_c and named as data package. For every data package, there is an overlapped address package with one cell spacing l_f over the data package in each direction for parallel operation and to improve the memory efficiency. For the narrow-band region, the level-set value is computed as the distance between the cells’ center to the geometry surface. While for the remaining area named as ‘far field’ in our method, only two fixed values $-4l_c$ and $4l_c$ are assigned with their memory addresses to each cell depending on whether the ‘far field’ cell is within the geometry or not. That means, in the narrow-band method, there are two levels of mesh, one covers the whole computational area with the coarse cell spacing l_c , the other is only employed in the narrow-band region with fine cell spacing l_f . The detailed implementation of our narrow-band and package techniques please refer to the Algorithm 1.

Algorithm 1: Algorithm for the construction of the level-set field with narrow-band and package techniques (in 2D)

```

1 Setup parameters and initialize the computation;
2 Read and parse the polygon mesh of a specific geometry from CAD files;
3 Divide calculation domain by a coarse cell spacing  $l_c$  into each  $C_{i,j}$ ;
4 Initialize the positive and negative far field cell  $C_p = 4l_c$  and  $C_n = -4l_c$ ;
5 forall  $C_{i,j}$  do
6   Detect the distance  $D_{i,j}$  of each coarse cell  $C_{i,j}$  to  $\Gamma_0$ ;
7   if  $D_{i,j} \leq l_c$  then
8     Mark  $C_{i,j}$  as Core_package and Inner_package;
9     Divide  $C_{i,j}$  by a fine cell spacing  $l_f$  into  $4 \times 4$  data_cells  $d_{m,n}$ ;
10    Initialize Core_package with  $\phi_{m,n}$  and its address;
11  else if  $C_{i,j} | \exists C_{i+i_0, j+j_0} \in \text{Core\_packages}, \wedge (\forall i_0, j_0 \in \{-1, 0, 1\})$  then
12    Mark  $C_{i,j}$  as Inner_package;
13    Divide  $C_{i,j}$  by a fine cell spacing  $l_f$  into  $4 \times 4$  data_cells  $d_{m,n}$ ;
14    Initialize Inner_package with  $\phi_{m,n}$  and its address;
15  else
16    Point the address of  $C_{i,j}$  to  $C_p$  or  $C_n$  depends on the sign of its
       $D_{i,j}$ ;
17  Link the address of each  $C_{i,j}$  of all Inner_packages;
18 end
19 forall Inner_packages do
20   Initialize the normal direction of each  $d_{m,n}$  by Eq.2;
21   Initialize the  $I_{i,j}$  of each  $d_{m,n}$  by Eq.21;
22 end
23 Terminate the computation.

```

2.2. Physics-driven particle relaxation

Isotropic and body-fitted particle distribution can be obtained by implementing a physics-driven relaxation process with a level-set based surface particle bounding [35]. In the physics-driven relaxation process, the particle advection is governed by

$$\frac{d\mathbf{v}}{dt} = \mathbf{F}_p, \quad (3)$$

where \mathbf{v} is the advection velocity, \mathbf{F}_p denotes the accelerations due to the repulsive pressure force and $\frac{d(\bullet)}{dt} = \frac{\partial(\bullet)}{\partial t} + \mathbf{v} \cdot \nabla(\bullet)$ stands for the material derivative. Following Refs. [35, 48, 49, 50], the pressure term in the right-hand-side of Eq.3 can be calculated as

$$\mathbf{F}_{p,a} = -\frac{2p_0 V_a}{m_a} \sum_b \nabla_a W_{ab} V_b, \quad (4)$$

by applying a constant background pressure p_0 [48]. Here, m is the particle mass, V the particle volume and $\nabla_a W_{ab}$ represents the gradient of the kernel

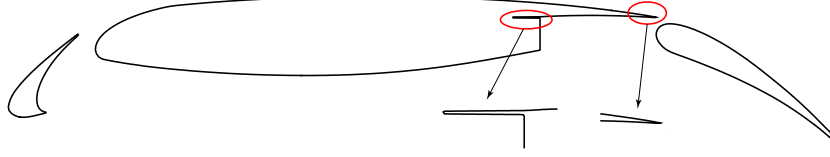


Figure 2: High-lift airfoil 30P30N with sharp trailing edge and a sharp slit at its second part.

function $W(|\mathbf{r}_{ab}|, h)$ with respect to particle a . Note that $\mathbf{r}_{ab} = \mathbf{r}_a - \mathbf{r}_b$ and h represents the smoothing length. Following with the time-step size Δt which is constrained by the body force criterion,

$$\Delta t \leq 0.25 \sqrt{\frac{h}{|\mathbf{d}\mathbf{v}/\mathbf{d}t|}}, \quad (5)$$

And the position updating method of particles as

$$\mathbf{r}^{n+1} = \mathbf{r}^n + \mathbf{d}\mathbf{r} = \mathbf{r}^n + \frac{1}{2} \mathbf{F}_p^n \Delta t^2. \quad (6)$$

To take into account the lack of kernel support for near-surface particles, the particle position is modified by a surface bounding

$$\mathbf{r}_a = \begin{cases} \mathbf{r}_a - (\phi_a + \frac{1}{2}\Delta x) \mathbf{N}_a & \phi_a \geq -\frac{1}{2}\Delta x \\ \mathbf{r}_a & \text{otherwise} \end{cases}, \quad (7)$$

where Δx denotes the particle spacing, and ϕ_a and \mathbf{N}_a are the level-set value and the normal direction at the position of particle a , respectively. More details are referred to Ref. [35].

3. ‘Dirty’ geometry cleaning

Here, we use a defective geometry of a high-lift airfoil 30P30N (shown in Fig. 2) to illustrate the issue of ‘dirty’ geometry. The airfoil has a typical sharp trailing edge and a small slit which is considered as a defect in its second part. These parts are left unresolved even very high resolution is applied. As shown in Fig. 3a, although the grid resolution used to generate lattice particle distribution is high enough compared to the chord length of the airfoil (0.002 to 1), several mono-layer particles are generated at the end of the sharp trailing edge with lattice distribution.

These mono-layer particles leads to unresolved singularity and can induce numerical instability during the relaxation process as shown in Fig. 3b, and failures of numerical simulations based on such particle distribution. Although increasing the resolution to fit the sharp non-resolved geometry could address this issue to some extent, excessive computational efforts are also inevitable. A possible solution is to clean up these non-resolved parts, as their impact on the simulation results under a given resolution very often is negligible.

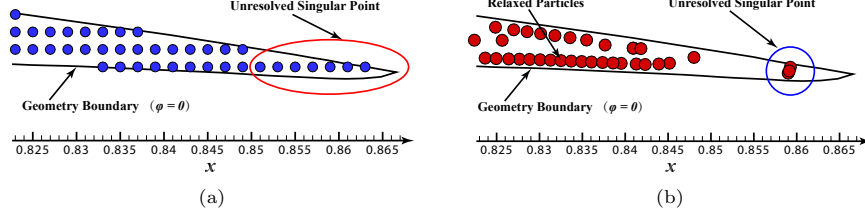


Figure 3: Unstable particle generation process caused by unsolved small structure. (a) Monolayer particles in trailing edge; (b) Unstable relaxation process.

3.1. Identify non-resolved small structures

Inspired by the scale separation method in Luo's work[51], an approach to finding the non-resolved structures of a geometry surface by detecting whether the mesh cell across zero level-set or an auxiliary level is employed in this paper (shown in Fig. 4). In order to distinguish different mesh cells, we call the mesh cells cut through by geometry surface Γ_0 the '0-cut-cells', represented by ' C_0 '.

$$C_0 = \{C_{i,j} | \exists \phi_{i\pm 1/2, j\pm 1/2} \cdot \phi_{i\pm 1/2, j\pm 1/2} < 0\}, \quad (8)$$

where $C_{i,j}$ is a mesh cell indexed by $[i, j]$ and $\phi_{i\pm 1/2, j\pm 1/2}$ is the level-set value at the corner of $C_{i,j}$, can be obtained by the following interpolation:

$$\begin{aligned} \phi_{i+1/2, j+1/2} &= \frac{1}{4}(\phi_{i,j} + \phi_{i+1,j} + \phi_{i,j+1} + \phi_{i+1,j+1}) \\ \phi_{i+1/2, j-1/2} &= \frac{1}{4}(\phi_{i,j} + \phi_{i+1,j} + \phi_{i,j-1} + \phi_{i+1,j-1}) \\ \phi_{i-1/2, j+1/2} &= \frac{1}{4}(\phi_{i,j} + \phi_{i-1,j} + \phi_{i,j+1} + \phi_{i-1,j+1}) \\ \phi_{i-1/2, j-1/2} &= \frac{1}{4}(\phi_{i,j} + \phi_{i-1,j} + \phi_{i,j-1} + \phi_{i-1,j-1}) \end{aligned} \quad (9)$$

Then the mesh cells cut through by positive auxiliary level Γ_+ and negative auxiliary level Γ_- are named as the 'positive-cut-cells' and the 'negative-cut-cells', respectively. Which yield

$$C_{+\epsilon} = \{C_{i,j} | \exists (\phi_{i\pm 1/2, j\pm 1/2} - \epsilon) \cdot (\phi_{i\pm 1/2, j\pm 1/2} - \epsilon) < 0\}, \quad (10)$$

$$C_{-\epsilon} = \{C_{i,j} | \exists (\phi_{i\pm 1/2, j\pm 1/2} + \epsilon) \cdot (\phi_{i\pm 1/2, j\pm 1/2} + \epsilon) < 0\}, \quad (11)$$

where ϵ is $0.75l_f$ as in Ref. [52].

Different from Luo's work [51], mesh cells which have the value of level-set between 0 and $-\epsilon$ ($0 > \phi > -\epsilon$) as well as those level-set value between 0 and $+\epsilon$ ($+\epsilon > \phi > 0$) must be found out and marked as 'gap-cut-cell'. This step is necessary, and the detailed explanation is given in section 3.2. According to the topological consistency, the mesh cells with a non-resolved geometry surface are those from ' C_0 ' and ' C_g ' but have only positive or negative auxiliary cells

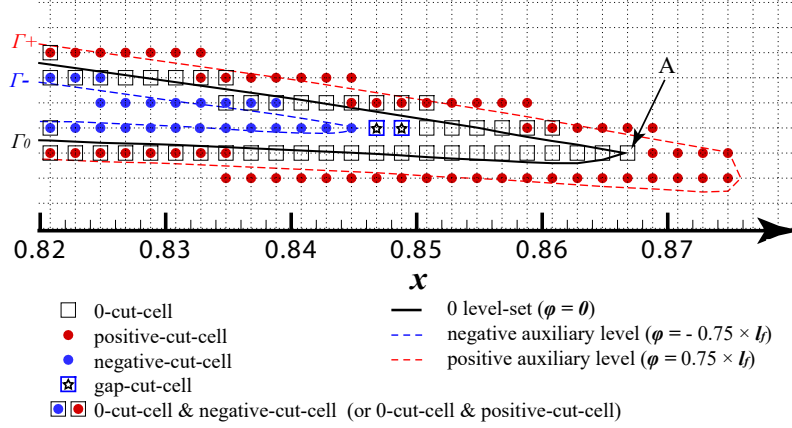


Figure 4: Mark non-resolved small structure. The 0-cut-cell ‘A’ has a 11 cell-spacing distance to nearest negative auxiliary level Γ_- , which is already far beyond its searching region, a 5×5 mesh cells area centered on ‘A’. Note that the background mesh are connected by the center of each cell.

as their neighbor cells. Note that the cut cell identifying operations only need to be executed in ‘core packages’.

$$C_{non-re} = \{C_{i,j} | C_{i,j} \in (C_0 \cup C_g) \wedge (\forall i_0, j_0 \in \{-1, 0, 1\}, C_{i+i_0, j+j_0} \notin (C_{+\epsilon} \cup C_{-\epsilon}))\} \quad (12)$$

For better understand, all the cut-cells marked by ‘ C_0 ’, ‘ $C_{+\epsilon}$ ’, ‘ $C_{-\epsilon}$ ’ and ‘ C_g ’ have a unified title ‘Interface ID’ in Algorithm 2.

3.2. level-set re-distance and reinitialize

To reconstruct the non-resolved geometry surface, one should modify the level-set value of those identified mesh cells with non-resolved segments. Inspired by the interface reconstruction method in Ref. [51], to facilitate the implementation, the non-resolved cut-cells C_{non-re} should be separated into two types, C_{non+} , which has no neighbors belonging to $C_{+\epsilon}$ within one cell-spacing distance from it:

$$C_{non+} = \{C_{i,j} | C_{i,j} \in (C_0 \cup C_g) \wedge (\forall i_0, j_0 \in \{-1, 0, 1\}, C_{i+i_0, j+j_0} \notin C_{+\epsilon})\}, \quad (13)$$

and C_{non-} , which has no neighbours belonging to $C_{-\epsilon}$ within one cell-spacing distance from it:

$$C_{non-} = \{C_{i,j} | C_{i,j} \in (C_0 \cup C_g) \wedge (\forall i_0, j_0 \in \{-1, 0, 1\}, C_{i+i_0, j+j_0} \notin C_{-\epsilon})\}. \quad (14)$$

According to Ref. [51], the level-set value of each re-distanced cut-cell in C_{non+} and C_{non-} is replaced by an estimated value of their distance to Γ_+ and Γ_- , respectively. However, as the geometry is relatively too sharp under a given resolution in many cases (Fig. 4), the Γ_+ or Γ_- is far from geometry boundary.

Considering that a large normal distance from the re-distanced cut-cell to a far-away auxiliary level is meaningless for resetting the level-set value, thus a searching region of 5×5 mesh cells area (in 2D) centered on the considered cut-cell is set by taking into account the computational efficiency. Meanwhile, a maximum replacement distance $D_{limit} = 3 \times l_f$ should also be given to prevent there being no corresponding auxiliary level in the search range, where the $3 \times l_f$ stands for a half cell-spacing beyond the searching radius, which means there is no auxiliary level in the searching region.

Then considering a cut cell ‘A’ in C_{non+} , one can get a normal ray pointing from the center of ‘A’ to the auxiliary level Γ_+ with an intersection point. The distance D between the cell center to the intersection point can be calculated by

$$D = \sqrt{(D_{cell-i} + \phi N_x)^2 + (D_{cell-j} + \phi N_y)^2}, \quad (15)$$

where the (D_{cell-i}, D_{cell-j}) are the cell distance in x and y direction between the considered cut cell ‘A’ in C_{non+} and a cell ‘P’ from auxiliary level $C_{+\epsilon}$ in the searching region respectively. (N_x, N_y) denotes the unit normal vector and ϕ is the level-set value of cell ‘P’. Then, the replaced level-set value for cut cell ‘A’ is:

$$\phi_{replace} = -\min(D_{min}, D_{limit}), \quad (16)$$

where D_{min} is the minimum value from Eq.15. When there is no auxiliary level in the searching region, D is considered infinite. Meanwhile, the replacement of the level-set value for a cut cell ‘B’ in C_{non-} can be obtained in the same way by only substituting $-\phi$ for ϕ in Eq.15 and the negative sign times the right side of Eq.16. Note that all the re-distance operations only need to be executed in ‘core packages’.

Here is an additional explanation of why the ‘gap-cut-cell’ is marked in the section 3.1. Considering some fairly sharp and narrow geometries, like the sharp trailing edge in Fig.4, the interval in x direction between Γ_0 and Γ_+ or Γ_- is relatively large compared with the distance in the vertical direction between two layers of Γ_+ or Γ_- in the sharp corner. Thus, the space between the new geometry surface and the auxiliary level (Γ_- or Γ_+) may be greater than one cell-spacing even replacing the level-set value of the non-resolved cut cell in the corner by D_{limit} . As shown in Fig. 4, the level-set value of the two cells in ‘ C_g ’ will not be changed during the re-distance process if they are not marked as non-resolved cut cells. Even though their right neighbor cells are the endpoints of the geometry surface, there is still a two-cell-spacing distance between Γ_0 and Γ_- , which does not conform to the topological consistency.

Since the level-set values may not be smooth after the re-distance operation, a re-initialization process is performed within the scope of ‘inner packages’ to achieve a continuous distribution of ϕ by the following equation [53]

$$\phi_\tau + sgn(\phi)(|\nabla\phi| - 1) = 0, \quad (17)$$

where τ is a pseudo time and $sgn(\phi)$ represents a sign function to maintain the signed distance property of level-set function.

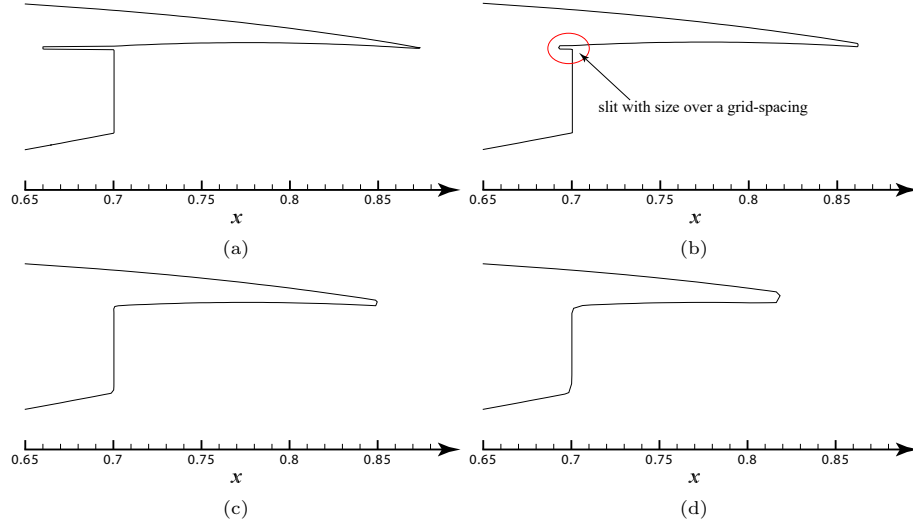


Figure 5: Airfoil surface reconstructed under different resolution. A small slit is added on the second part of the airfoil mimics a defect in the geometric model. (a) Original geometry surface; (b) Reconstructed with resolution 0.001; (c) Reconstructed with resolution 0.002; (d) Reconstructed with resolution 0.005.

Fig. 5 shows the reconstructed geometry surface under different resolutions. A small slit is added to the second part of the high-lift airfoil 30P30N to mimic a defect in the geometric model. Together with the original sharp trailing edge (shown in Fig. 5a), these non-resolved geometry fragments under a given resolution need to be reconstructed before particle or mesh generation. At a relatively high resolution, the rear part of the small slit is not recognized as the non-resolved segment since the width of this part is beyond a cell-spacing, and there is a tiny slit left at the corner between the airfoil tail and the main body as shown in Fig. 5b. However, the non-resolved sharp trailing edge is reconstructed with a smoothed filleted corner which has a minimum size larger or equal to two cell-spacing. With the decreasing of the resolution (from Fig. 5b to Fig. 5d), more portion of the trailing edge is identified as a non-resolved segment and reconstructed. When the small slit is completely cleaned up at the resolution of 0.002, no additional variation at this area of the geometric surface presents. This can prove that the present reconstruction process will automatically stop as the topological consistency is satisfied.

Figure 6 shows the lattice particle distribution at the trailing edge of the airfoil after reconstructing the non-resolved geometric surface. It can be observed that the single layer unresolved singular points (shown as grey dots in Fig. 6) are vanished compared with Figure 3a. The two points on different layers at the far left of those removed particles are also included, which is due to the cells in ‘ C_g ’ being recognized as unresolved fragments. The ‘dirty’ geometry clean-up process is illustrated in Algorithm 2.

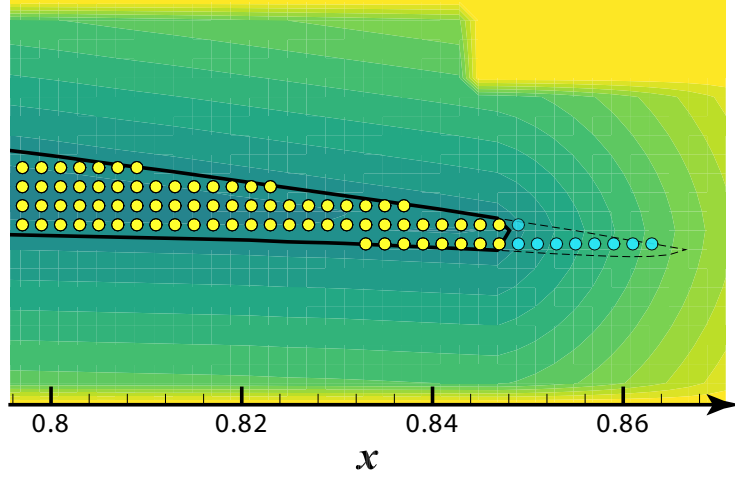


Figure 6: Lattice particles generated after clean the non-resolved structure. The grey dots represent those unresolved singular points but vanished after the clean process.

Algorithm 2: Algorithm for ‘dirty’ geometry clean-up

```

1 if Geometry needs to be clean then
2   for all Core_packages do
3     Mark  $InterfaceID_{(m,n)}$  of every  $d_{m,n}$ ;
4     Find out the cut-cells  $\in C_{non-re}$  ;
5     Re-distance the  $\phi_{m,n}$  for cut-cells  $\in C_{non+}$  and  $\in C_{non-}$ 
      respectively according to Eq.15 and Eq.16;
6   end
7   for all Inner_packages do
8     Reinitialize the  $\phi_{m,n}$  of each  $d_{m,n}$  by Eq.17;
9     Update the normal direction of each  $d_{m,n}$  by Eq.2;
10    Update the  $I_{i,j}$  of each  $d_{m,n}$  by Eq.21;
11  end
12 Terminate the simulation.

```

4. ‘Static confinement’ boundary condition

As mentioned in the introduction, the simple bounding method [35] constraints the particles within the geometry using level-set value and the normal direction. But the particles near the geometry surface still have an incomplete support domain during the physics-driven relaxation process. This will not lead to a serious problem to those geometric surfaces with smooth shapes and small curvature. As shown in Fig.7, without the complete kernel support, although the relaxation process converges, the boundary particles have a smaller particle spacing comparing with inner particles. This will cause a slight inconsistency between particle distribution and particle volume. However, for those geome-

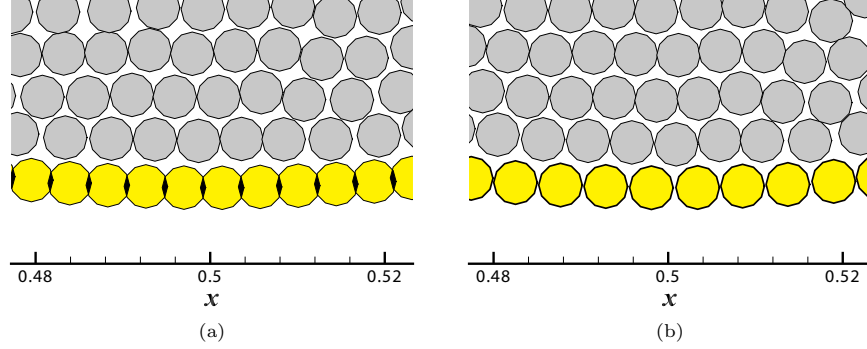


Figure 7: Boundary particle distribution of a circle without ‘static confinement’ (a) and with ‘static confinement’ (b). Note that without ‘static confinement’ boundary condition, the (yellow) particle at the outer layer exhibit smaller distances than inner (gray) particles.

tries with greater curvature and sharp features, the particle relaxation may not converge with incomplete kernel support. It is clearly shown in a snapshot of particle distribution in Fig. 8a, where a few particles at the very end of the airfoil trailing edge are on the position where the particle relaxation does not converge, but with persistent cycling motion. In order to address the above-mentioned issue, here, we propose a method based on the level-set field to achieve full kernel support, which is denoted as ‘static confinement’.

We first consider an ideal situation in which a considered near-surface particle a locates at a cell center, as illustrated in Fig. 9. As its kernel support partially within the surface, and partially from the outside region, the particle approximation of a derivative ∇f_a can be obtained by

$$\nabla f_a \approx \sum_{b, \phi_b < 0} f_b \nabla W_{ab} V_b + \sum_{c, \phi_c > 0} f_c \nabla W_{ac} V_c, \quad (18)$$

where the second term of the right-hand-side provides the support outside of the surface, c represent the cell centers of the level set mesh within the cut-off radius from a and V_c are the volume outside of the surface in each mesh cell. If this approximation is used for particle relaxation as Eq.3, one can obtain

$$\mathbf{F}_{p,a} = -\frac{2p_0 V_a}{m_a} \left(\sum_{b, \phi_b < 0} \nabla W_{ab} V_b + \sum_{c, \phi_c > 0} \nabla W_{ac} V_c \right). \quad (19)$$

Note that, here, for the volume contribution of each cell near the surface to the extra term introduced in Eq. 19, we simply divide the level-set meshes in the support domain into three categories as shown in Fig. 9. The first type is the cells inside both the geometry and cut-off region but not cross by geometry surface(Γ_0), which have no contribution to the kernel support. The second type is the cells inside the cut-off region and cross by geometry surface(Γ_0), which have partial volume (the part outside geometry) to complete the kernel support.

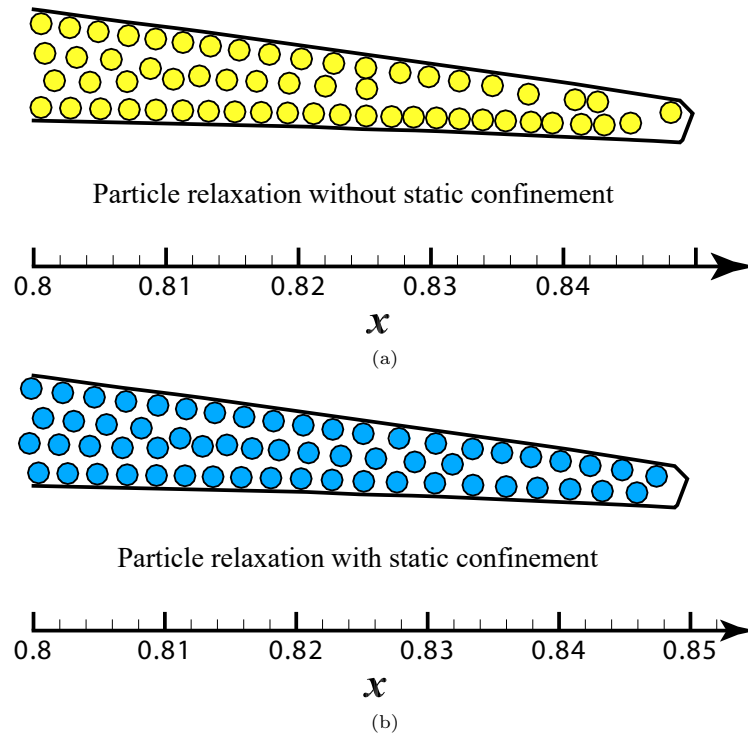


Figure 8: Particle distribution at trailing edge without static confinement (a) and with static confinement (b) .

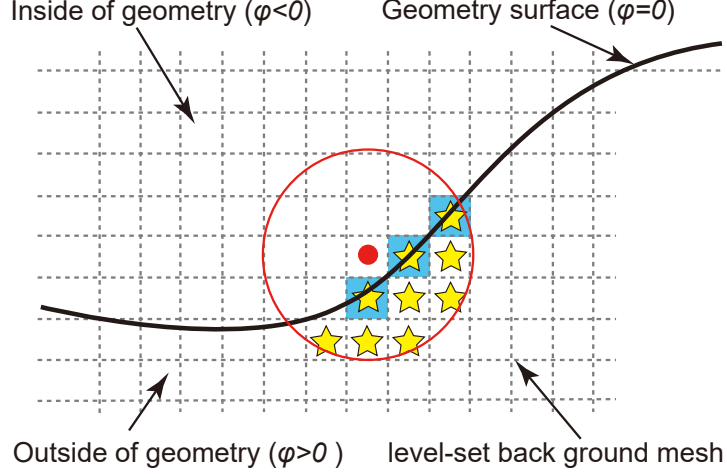


Figure 9: ‘Static confinement’ method for completing kernel of boundary particles. The red circle line is the cut-off region of the red particle a near the geometry surface. The white cells inside the geometry and the cut-off region have no contribution to complete the kernel support for the particle a . The blue cells with a yellow star have the partial volume to complete the kernel support for the particle a . The white cells with a yellow star have full volume contributing to the kernel support for the particle a . Note that the particle a is just located on the cell-center of the background level-set mesh.

The last type is the cells that are fully outside geometry but inside the cut-off region, which have their volume contributed to replenishing the kernel support completely. With the level-set method [54, 53], the volume fraction for the part outside geometry corresponding to $\phi > 0$ of each cell can be estimated by the smoothed Heaviside function

$$H(\phi, \epsilon) = \begin{cases} 0 & \phi < -\epsilon \\ \frac{1}{2} + \frac{\phi}{2\epsilon} + \frac{1}{2\pi} \sin\left(\frac{\pi\phi}{\epsilon}\right) & -\epsilon < \phi < \epsilon \\ 1 & \phi > \epsilon \end{cases} \quad (20)$$

Then, the extra term in Eq. 20 can be rewritten as

$$I_{i,j} = \sum_{c, \phi_c > 0} \nabla W_{ac} V_c = \sum_{c, \phi_c > 0} H(\phi_c, \epsilon) l_f^m \nabla_a W_{ac}, \quad (21)$$

here the l_f^m , m is dimension, denotes the volume of each computational cell, (i, j) denotes the cell index.

Note that Eq. 19 is only validate when the particles a locates on a mesh center. For the particle-relaxation process, one need the value of the extra term $I_{i,j}$ when the particles locates at a general position. Also note that, this extra term is only dependent on the position (i, j) and the surface location, which is fixed during the relaxation process. Therefore, one can first simply compute the values of $I_{i,j}$ at all cell centers near the surface, and then obtained the value at

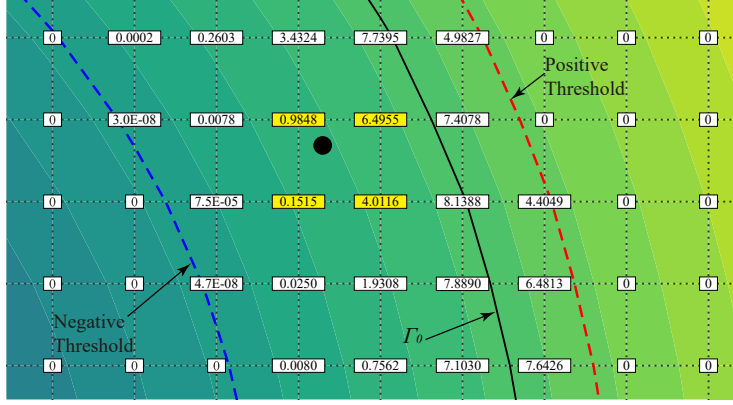


Figure 10: Implementation of the ‘static confinement’ condition. The value of $I_{i,j}$ for the black inner particle can be interpolated from the four values (in yellow boxes) around it. The negative threshold $T_n = -(r_c + l_f)$ and the positive threshold $T_p = l_f$ on both sides of Γ_0 is set for improving the computational efficiency. Here r_c is the cut-off radius and l_f is the cell-spacing as mentioned in Sec 2.1. Setting T_p as one cell-spacing beyond the geometry is only for the interpolation when the boundary particle is in the cut cell which is crossed by Γ_0 .

an arbitrary particle position, with the standard bi- or tri-linear interpolation during the relaxation process, (as shown in Fig. 10).

By imposing the ‘static confinement’ as the boundary condition for physics-driven relaxation process, the distribution of the outer layer particles is significantly improved as shown in Fig. 7b. By comparing Fig. 7a with Fig. 7b, it is observed that the outer layer particles can get the same particle spacing as the inner particles when the ‘static confinement’ is employed. Also, the particles near very sharp features can obtain a better body-fitted distribution as shown in Fig. 8b. The body-fitted particle generation workflow with ‘static confinement’ boundary condition is presented in Algorithm 3.

5. Numerical Examples

In this section, the convergence analysis of average kinetic energy is carried out to verify that, without clean-up the non-resolved singular points, the physics-driven simulation cannot achieve the steady-state and the convergence. In addition, the particle distributions of several complex 3D geometries with small structures are exhibited to show the ‘dirty’ geometry clean-up ability of the present pre-processing tool, as well as to reveal the importance of a cleaned geometry for industry applications.

In present work, all the simulations below are carried out on an Intel Core(TM) CPU i9-9900 3.10GHZ Desktop computer with 64GB RAM and Windows 10 system.

Algorithm 3: Algorithm for physics-driven relaxation particle generation with ‘static confinement’

```

1 Setup parameters and initialize the physics-driven relaxation;
2 Run Algorithm 1;
3 if Geometry needs to be clean then
4   | Run Algorithm 2;
5 end
6 Generate a preconditioned lattice particle distribution;
7 while simulation termination condition is not satisfied do
8   | Get  $I_{i,j}$  of each particle by trilinear interpolation;
9   | Calculate the pressure force  $\mathbf{F}_p$  according to Eq. (19);
10  | Set the time-step  $\Delta t$  according to Eq. (5);
11  | Update particles position  $\mathbf{r}^{n+1}$  according to Eq. (6);
12  | Get level-set value  $\phi_a$  and normal direction  $\mathbf{N}_a$  of each particle by
    | trilinear interpolation;
13  | Constrain particles onto surface according to Eq. (7);
14  | Update the particle-neighbor list and kernel values and gradient ;
15  | Update the particle configuration ;
16 end
17 Terminate the simulation.

```

5.1. 2D airfoil 30P30N

As we mentioned in the previous section, the physics-driven process is not numerically stable and can not achieve the convergent result if there is a non-resolved singular structure present. In this section, we consider particle generation for an original 2D airfoil 30P30N to qualitatively and quantitatively demonstrate the stability and convergence of the present method.

Fig. 11 shows the particle distribution at the trailing edge of the airfoil obtained by the physics-driven relaxation process with and without clean-up non-resolved structure under a normalized resolution of 0.001. As shown in Fig. 11a, there are still several singular particles at the end of the trailing edge that can not reach a stable state during the physics-driven relaxation process, free from the main body of the trailing edge and agglomerate together even with a relatively high resolution. In contrast, the particles achieve quite good body-fitted distribution on the trailing edge after cleaning up the non-resolved small fragment as shown in Fig. 11b.

Fig. 12 illustrates the time history of the average kinetic energy during the physics-driven relaxation process with and without clean-up of non-resolved structure. To better explain the numerical unstable process, three different normalized resolutions related to the airfoil chord are adopted in this test. The three jittery curves in Fig. 12a show that the physics-driven relaxation process is unstable and can not achieve the convergent result as the presence of a non-resolved structure. As the resolution decreases, the instability becomes more and more severe. In particular, the average kinetic energy curve can not even reach a

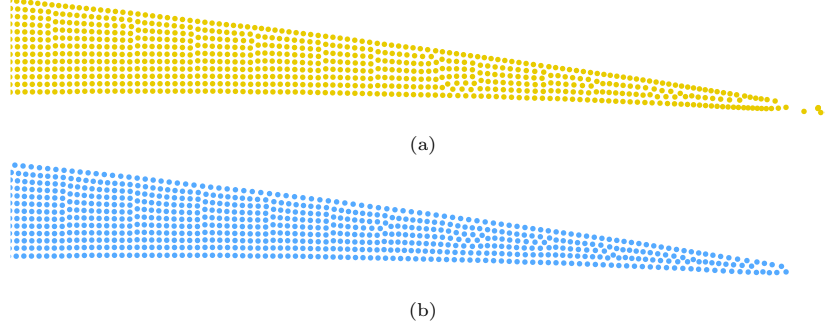


Figure 11: Particle distribution on trailing edge of the airfoil under the normalized resolution 0.001: (a) Without clean-up non-resolved structure; (b) With clean-up non-resolved structure.

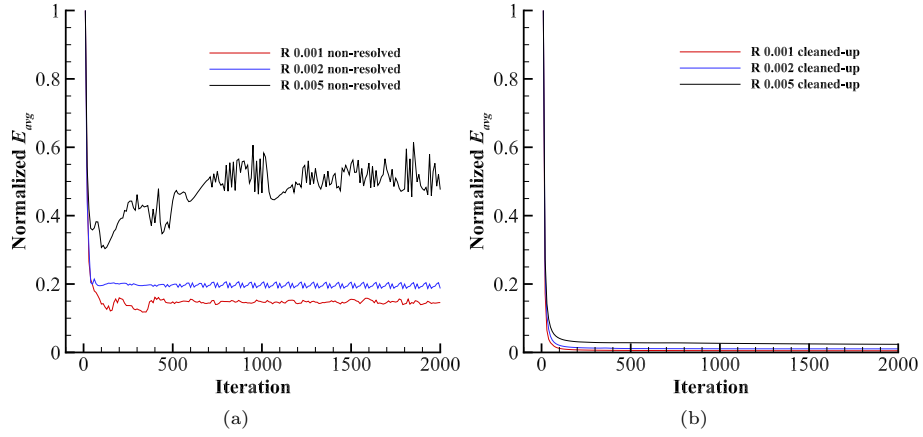


Figure 12: Average particle kinetic energy during the physics-driven relaxation process: (a) Without clean-up non-resolved structure; (b) With clean-up non-resolved structure.

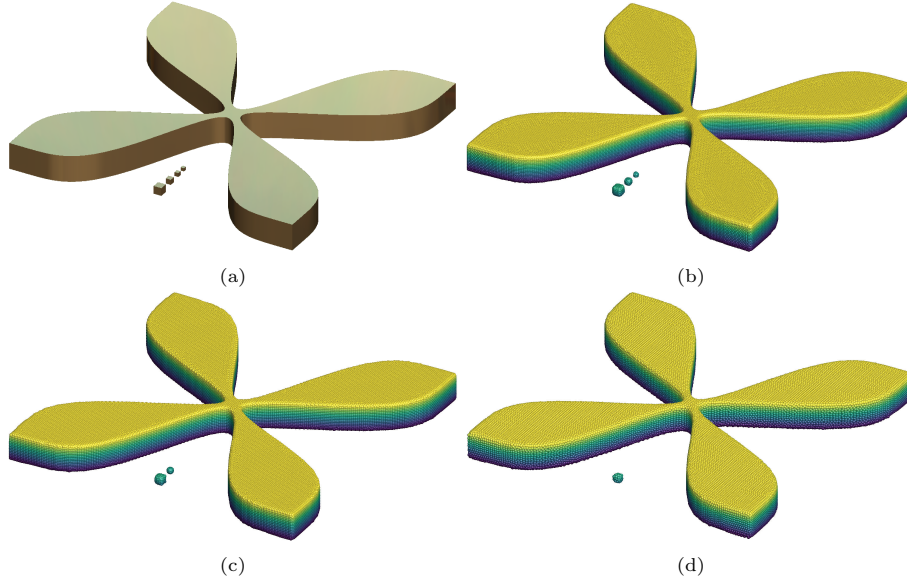


Figure 13: Schematic geometry and particles distributions under different spatial resolutions for the 3D SPHinXsys symbol. (a) Original geometry surface; (b) Reconstructed with resolution 0.02; (c) Reconstructed with resolution 0.025; (d) Reconstructed with resolution 0.032

state of periodic oscillation when the resolution reduces to 0.005. A coarser grid resolution would result in more trailing edge parts with thickness less than a cell-spacing, thus generating more mono-layer singular particles. As mentioned before, these mono-layer singular particles are the reason for instability and even failure to converge. As a comparison in Fig. 12b, after the peak value in the initial status, all the three average kinetic energy curves drop rapidly and tend to be stable after 100 iterations with clean-up non-resolved structure.

5.2. SPHinXsys symbol with small structures

With the development of 3D scanning technology, many geometric models can be obtained through 3D scanning. However, the scanning process may generate some small structures that are free of the main body. These small structures bring challenge for mesh or particle generation for computational aspects. In this part, we consider generating a particle model for the 3D symbol of our SPHinXsys project with some small structures to validate the performance of the present pre-processing tool for automatically identifying and cleaning up the non-resolved small structures free from the main body under diverse spatial resolutions. The schematic geometry of the SPHinXsys symbol with small structures are shown in Fig. 13a. The size of 3D SPHinXsys symbol is about $4.4 \times 4.4 \times 0.4$, together with four small structures of different sizes which are free between the two leaves of the main structure.

Fig. 13 also shows the particle distributions for the SPHinXsys symbol with different resolutions, which are 0.02, 0.025 and 0.032 with respect to x

Table 1: Computational burden comparison among different resolutions of the skyscraper

Normalized Resolution	Particles QTY (million)	Level-set Time (s)	Particle Generation Time (s)	Iteration Time (s)
0.08	0.271	13.10	0.10	145.98
0.05	1.559	54.08	0.53	900.38
0.03	4.873	145.28	1.70	2874.13

direction. It is clear that, with decreasing resolution, the free small structures are cleaned-up accordingly. Meanwhile, the main body is completely preserved and body-fitted particle distributions are obtained. In addition, the free small structures that can be resolved at the corresponding resolution also produce a body-fitting particle distribution. Note that no matter how the resolution is modified, the main body of the geometric model is constant, implying the consistent feature of a cleaning tool for ‘dirty’ geometry.

5.3. Skyscraper with a flagpole

In this part, a geometric model of a skyscraper with a flagpole is applied to test the impact of capturing the small structure on the computational burden. The whole computational domain of the skyscraper is about $6 \times 6 \times 21.6$ and it includes a two-section flagpole with different diameters. The numerical simulations involving this kind of building structure are usually aiming at structural strength testing and vibration amplitude detection. Thus the flagpoles do not play a decisive influence in the simulation and can be removed.

Table 1 presents the computational burden comparison when different resolutions are adopted to the numerical simulation of the skyscraper model. The numerical process in this example is the physics-driven particle generation process. The involved level-set operations are level-set initialization, ‘dirty’ geometry cleaning-up, and level-set re-initialization. The ‘Particle Generation Time’ is the real-time of lattice distributed particle generation. While the ‘Iteration Time’ is the real-time for 1000 iteration steps of the relaxation process. The normalized resolutions related to x direction are set as 0.03, 0.05 and 0.08 respectively in order to keep the geometric structure in three different states (Corresponding to Fig. 14b to Fig. 14d). From the table, it is clear that the computational burden and calculation time will explosively increase only to capture an insignificant small structure. Fig. 14 further illustrates the reconstructed skyscraper features at different resolutions and their particle distributions. By omitting different levels of flagpole structure, the number of particles in the skyscraper model has been greatly reduced. At the same time, its main body is still maintained.

5.4. Inferior vena cava

In this section, we consider an inferior vena cava where several branches with different diameters are present to test the ability of the proposed method to preserve the small structure on the main body under a given resolution.

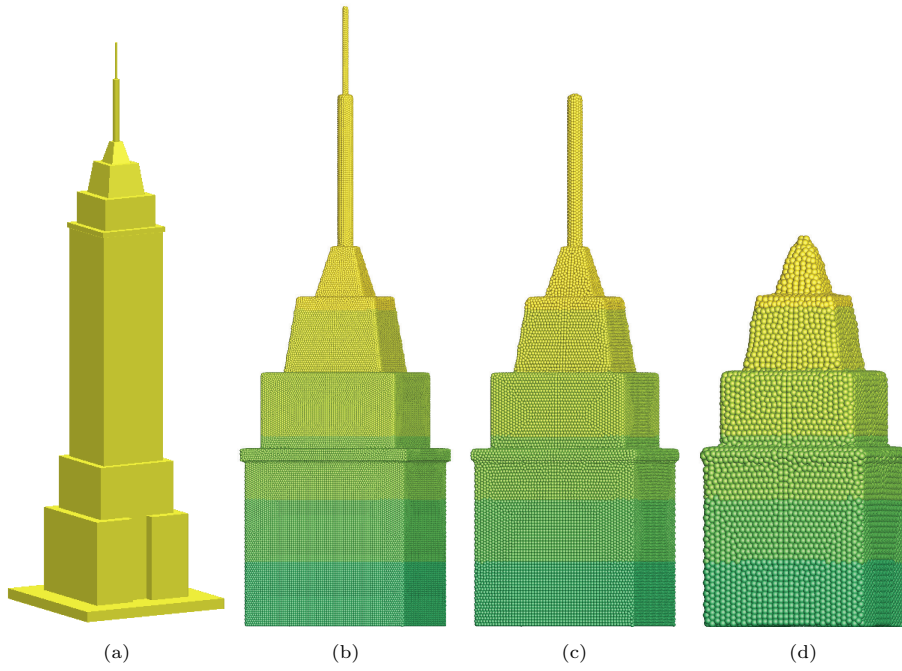


Figure 14: The reconstructed geometry surface and particle distribution of a skyscraper under different resolution : (a) Original geometry model, (b) Reconstructed at resolution of 0.03, (c) Reconstructed at resolution of 0.05 and (d) Reconstructed at resolution of 0.08.

The size of this inferior vena cava is around $180 \times 465 \times 33$ and its schematic geometry is shown in Fig. 15a. Generally, this kind of tree structure has many small branches with different diameters. For the force study of the main body, these small branches will have no effect but increase the computational burden. Therefore, those small branches, which cannot be resolved at a given resolution, should be removed. While those resolved branches should be kept in the main body at that resolution.

Fig. 15 shows the reconstructed inferior vena cava geometries under different resolutions, i.e., 1.35, 1.0 and 0.55 with respect to x direction, and the corresponding particle distribution. On the original geometry there are several small branches with different diameters attached to the main vessel. As the resolution decreases from 0.55 to 1.35 (from Fig. 15b to Fig. 15d), the small branches are gradually cleaned up. However, the main blood vessels of the inferior vena cava are still preserved and a body-fitted particle distribution is generated.

6. Concluding remarks

In this paper, we have developed the level-set based pre-processing techniques for particle-based methods. Firstly, the ‘dirty’ geometry cleaning technique can automatically detect and remove the non-resolved small structures of ‘dirty’ geometries at a given grid resolution. A number of numerical tests are demonstrated to validate the ‘dirty’ geometry cleaning-up ability of our pre-processing tool. The cleaning algorithm of our method can not only identify and clean-up the non-resolved small structures but also automatically stop cleaning at the main body which has topological consistency. In addition, a level-set based ‘static confinement’ boundary condition is developed to complete the kernel support in the physics-driven relaxation process. By calculating the missing part of kernel support and storing it in the background level-set cell center, the physics-driven relaxation process obtains the full kernel support for particles close to the surface. This allows for better optimization of boundary particle distribution, even for those with sharp geometries.

7. Acknowledgement

Y.C. Yu is fully supported by the China Scholarship Council (CSC) (No:201806120023). C. Zhang and X.Y. Hu would like to express their gratitude to Deutsche Forschungsgemeinschaft for their sponsorship of this research under grant number DFG HU1527/12-4.

CRedit authorship contribution statement

Yongchuan Yu: Investigation, Methodology, Visualization, Validation, Formal analysis, Writing - original draft, Writing - review & editing; **Yujie Zhu:** Investigation, Methodology, Formal analysis, Writing - review & editing; **Chi Zhang:** Investigation, Methodology, Formal analysis, Writing - review &

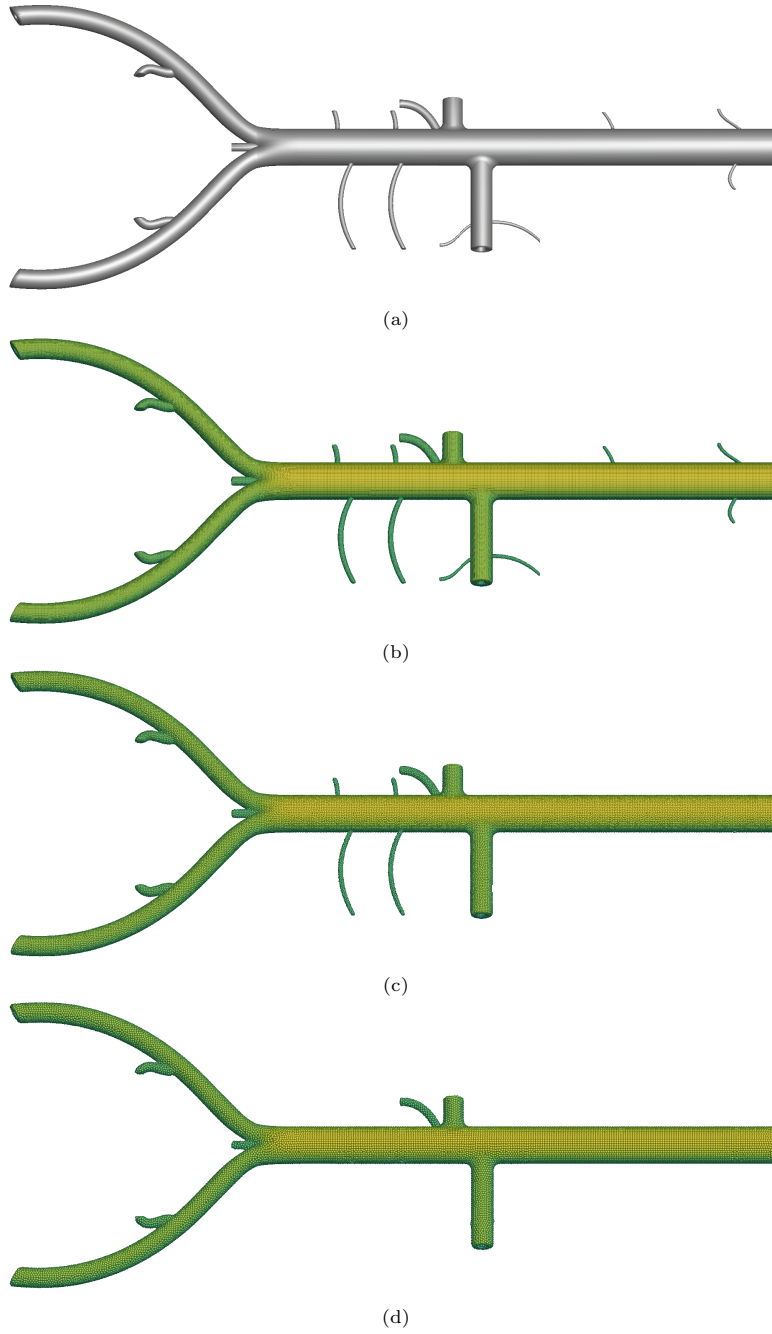


Figure 15: Particle distributions under different resolutions for reconstructed small branches of the inferior vena cava. (a) Original geometry; (b) Reconstructed with resolution 0.55; (c) Reconstructed with resolution 1.0; (d) Reconstructed with resolution 1.35.

editing; **Oskar J. Haidn:** Investigation, Supervision, Writing - review & editing. **Xiangyu Hu:** Investigation, Methodology, Supervision, Writing - review & editing;

Declaration of competing interest

The authors declare that they have no known competing financial interests or personal relationships that could have appeared to influence the work reported in this paper.

References

- [1] A. Xenakis, S. Lind, P. Stansby, B. D. Rogers, Landslides and tsunamis predicted by incompressible smoothed particle hydrodynamics (sph) with application to the 1958 lituya bay event and idealized experiment, *Proceedings of the Royal Society A: Mathematical, Physical and Engineering Sciences* 473 (2199) (2017) 20160674.
- [2] P. W. Cleary, S. M. Harrison, M. D. Sinnott, G. G. Pereira, M. Prakash, R. C. Cohen, M. Rudman, N. Stokes, Application of sph to single and multiphase geophysical, biophysical and industrial fluid flows, *International Journal of Computational Fluid Dynamics* (2020) 1–57.
- [3] P. W. Cleary, M. Prakash, S. Mead, X. Tang, H. Wang, S. Ouyang, Dynamic simulation of dam-break scenarios for risk analysis and disaster management, *International Journal of Image and Data Fusion* 3 (4) (2012) 333–363.
- [4] C. Zhang, J. Wang, M. Rezavand, D. Wu, X. Hu, An integrative smoothed particle hydrodynamics method for modeling cardiac function, *Computer Methods in Applied Mechanics and Engineering* 381 (2021) 113847.
- [5] S. M. Harrison, R. C. Cohen, P. W. Cleary, S. Barris, G. Rose, A coupled biomechanical-smoothed particle hydrodynamics model for predicting the loading on the body during elite platform diving, *Applied Mathematical Modelling* 40 (5-6) (2016) 3812–3831.
- [6] N. Tanaka, T. Takano, Microscopic-scale simulation of blood flow using sph method, *International Journal of Computational Methods* 2 (04) (2005) 555–568.
- [7] C. Zhang, Y. Zhu, Y. Yu, D. Wu, M. Rezavand, S. Shao, X. Hu, An artificial damping method for total lagrangian sph method with application in biomechanics, *Engineering Analysis with Boundary Elements* 143 (2022) 1–13.
- [8] A. Leroy, A new incompressible sph model: towards industrial applications, Ph.D. thesis, Université Paris-Est (2014).
- [9] P. Groenenboom, B. Cartwright, D. McGuckin, O. Amoignon, M. Mettichi, Y. Gargouri, A. Kamoulakos, Numerical studies and industrial applications of the hybrid sph-fe method, *Computers & Fluids* 184 (2019) 40–63.
- [10] M. S. Shadloo, G. Oger, D. Le Touzé, Smoothed particle hydrodynamics method for fluid flows, towards industrial applications: Motivations, current state, and challenges, *Computers & Fluids* 136 (2016) 11–34.
- [11] M. Lavoie, A. Gakwaya, M. N. Ensan, Application of the sph method for simulation of aerospace structures under impact loading, in: *Proceedings of the 10th International LSDYNA Users Conference*, Dearborn, Michigan, 2008.

- [12] M. Siemann, S. A. Ritt, Novel particle distributions for sph bird-strike simulations, *Computer Methods in Applied Mechanics and Engineering* 343 (2019) 746–766.
- [13] R. Ortiz, J. Charles, J. Sobry, Structural loading of a complete aircraft under realistic crash conditions : Generation of a load database for passenger safety and innovative design, 2004.
- [14] C. Zhang, Y. Wei, F. Dias, X. Hu, An efficient fully lagrangian solver for modeling wave interaction with oscillating wave surge converter, *Ocean Engineering* 236 (2021) 109540.
- [15] M. Luo, A. Khayyer, P. Lin, Particle methods in ocean and coastal engineering, *Applied Ocean Research* 114 (2021) 102734.
- [16] G. Cai, M. Luo, A. Khayyer, X. Zhao, Sph simulation of wave impact on coastal bridge piers, in: *The 32nd International Ocean and Polar Engineering Conference*, OnePetro, 2022.
- [17] K. Pan, R. IJzermans, B. Jones, A. Thyagarajan, B. van Beest, J. Williams, Application of the sph method to solitary wave impact on an offshore platform, *Computational Particle Mechanics* 3 (2) (2016) 155–166.
- [18] A. Nassiri, B. Kinsey, Numerical studies on high-velocity impact welding: smoothed particle hydrodynamics (sph) and arbitrary lagrangian–eulerian (ale), *Journal of Manufacturing Processes* 24 (2016) 376–381.
- [19] C. Ndimande, P. Cleary, A. Mainza, M. Sinnott, Using two-way coupled dem-sph to model an industrial scale stirred media detritor, *Minerals Engineering* 137 (2019) 259–276.
- [20] J. Dominguez, A. Crespo, A. Barreiro, M. Gesteira, A. Mayrhofer, Development of a new pre-processing tool for sph models with complex geometries, in: *6th international SPHERIC workshop*, 2011.
- [21] F. Wang, Z. Sun, Y. Sun, K. Zhang, G. Xi, Simulation of a centrifugal pump based on a lagrangian particle solver, *Journal of Fluids Engineering* 144 (6), 061105 (02 2022).
- [22] A. Colagrossi, B. Bouscasse, M. Antuono, S. Marrone, Particle packing algorithm for sph schemes, *Computer Physics Communications* 183 (8) (2012) 1641–1653.
- [23] Y.-X. Peng, A.-M. Zhang, F.-R. Ming, S.-P. Wang, A meshfree framework for the numerical simulation of elasto-plasticity deformation of ship structure, *Ocean Engineering* 192 (2019) 106507.
- [24] L. Han, X. Hu, Sph modeling of fluid-structure interaction, *Journal of Hydrodynamics* 30 (1) (2018) 62–69.

- [25] M. Liu, Z. Zhang, Smoothed particle hydrodynamics (sph) for modeling fluid-structure interactions, *Science China Physics, Mechanics & Astronomy* 62 (8) (2019) 984701.
- [26] C. Zhang, M. Rezavand, X. Hu, A multi-resolution sph method for fluid-structure interactions, *Journal of Computational Physics* 429 (2021) 110028.
- [27] G. Fourtakas, P. Stansby, B. D. Rogers, S. Lind, An eulerian–lagrangian incompressible sph formulation (eli-sph) connected with a sharp interface, *Computer Methods in Applied Mechanics and Engineering* 329 (2018) 532–552.
- [28] A. Nasar, B. D. Rogers, A. Revell, P. Stansby, S. Lind, Eulerian weakly compressible smoothed particle hydrodynamics (sph) with the immersed boundary method for thin slender bodies, *Journal of Fluids and Structures* 84 (2019) 263–282.
- [29] S. Diehl, G. Rockefeller, C. L. Fryer, D. Riethmiller, T. S. Statler, Generating optimal initial conditions for smoothed particle hydrodynamics simulations, *Publications of the Astronomical Society of Australia* 32 (2015).
- [30] P. Groenenboom, Particle filling and the importance of the sph inertia tensor, in: *Proceedings of 9th International SPHERIC Workshop*, Paris, France, 2014.
- [31] M. Siemann, P. Groenenboom, Modeling and validation of guided ditching tests using a coupled sph-fe approach, in: *Proceedings of 9th International SPHERIC Workshop*, Paris, France, 2014.
- [32] L. Fu, L. Han, X. Y. Hu, N. A. Adams, An isotropic unstructured mesh generation method based on a fluid relaxation analogy, *Computer Methods in Applied Mechanics and Engineering* 350 (2019) 396–431.
- [33] Z. Ji, L. Fu, X. Hu, N. Adams, A consistent parallel isotropic unstructured mesh generation method based on multi-phase sph, *Computer Methods in Applied Mechanics and Engineering* 363 (2020) 112881.
- [34] Z. Ji, L. Fu, X. Hu, N. Adams, A feature-aware sph for isotropic unstructured mesh generation, *Computer Methods in Applied Mechanics and Engineering* 375 (2021) 113634.
- [35] Y. Zhu, C. Zhang, Y. Yu, X. Hu, A cad-compatible body-fitted particle generator for arbitrarily complex geometry and its application to wave-structure interaction, *Journal of Hydrodynamics* 33 (2021) 195–206.
- [36] J. R. Chawner, J. Dannenhoffer, N. J. Taylor, Geometry, mesh generation, and the cfd 2030 vision, in: *46th AIAA Fluid Dynamics Conference*, 2016, p. 3485.

- [37] K. Onishi, M. Tsubokura, Topology-free immersed boundary method for incompressible turbulence flows: An aerodynamic simulation for “dirty” cad geometry, *Computer Methods in Applied Mechanics and Engineering* 378 (2021) 113734.
- [38] T. Long, D. Hu, D. Wan, C. Zhuang, G. Yang, An arbitrary boundary with ghost particles incorporated in coupled fem–sph model for fsi problems, *Journal of Computational Physics* 350 (2017) 166–183.
- [39] H. Schechter, R. Bridson, Ghost sph for animating water, *ACM Transactions on Graphics (TOG)* 31 (4) (2012) 1–8.
- [40] L. V. Vela, J. M. Reynolds-Barredo, R. Sánchez, A positioning algorithm for sph ghost particles in smoothly curved geometries, *Journal of Computational and Applied Mathematics* 353 (2019) 140–153.
- [41] C. Zhang, M. Rezavand, Y. Zhu, Y. Yu, D. Wu, W. Zhang, S. Zhang, J. Wang, X. Hu, Sphinxsys: An open-source meshless, multi-resolution and multi-physics library, *Software Impacts* 6 (2020) 100033.
- [42] C. Zhang, M. Rezavand, Y. Zhu, Y. Yu, D. Wu, W. Zhang, J. Wang, X. Hu, Sphinxsys: an open-source multi-physics and multi-resolution library based on smoothed particle hydrodynamics, *Computer Physics Communications* (2021) 108066.
- [43] M. A. Sherman, A. Seth, S. L. Delp, Simbody: multibody dynamics for biomedical research, *Procedia Iutam* 2 (2011) 241–261.
- [44] D. Adalsteinsson, J. A. Sethian, A fast level set method for propagating interfaces, *Journal of computational physics* 118 (2) (1995) 269–277.
- [45] P. Gomez, J. Hernandez, J. Lopez, On the reinitialization procedure in a narrow-band locally refined level set method for interfacial flows, *International journal for numerical methods in engineering* 63 (10) (2005) 1478–1512.
- [46] J. Ye, I. Yanovsky, B. Dong, R. Gandlin, A. Brandt, S. Osher, Multigrid narrow band surface reconstruction via level set functions, in: *International Symposium on Visual Computing*, Springer, 2012, pp. 61–70.
- [47] L. Han, X. Hu, N. A. Adams, Adaptive multi-resolution method for compressible multi-phase flows with sharp interface model and pyramid data structure, *Journal of Computational Physics* 262 (2014) 131–152.
- [48] S. Litvinov, X. Hu, N. A. Adams, Towards consistence and convergence of conservative sph approximations, *Journal of Computational Physics* 301 (2015) 394–401.
- [49] S. Adami, X. Hu, N. A. Adams, A transport-velocity formulation for smoothed particle hydrodynamics, *Journal of Computational Physics* 241 (2013) 292–307.

- [50] C. Zhang, X. Y. Hu, N. A. Adams, A generalized transport-velocity formulation for smoothed particle hydrodynamics, *Journal of Computational Physics* 337 (2017) 216–232.
- [51] J. Luo, X. Hu, N. A. Adams, Efficient formulation of scale separation for multi-scale modeling of interfacial flows, *Journal of Computational Physics* 308 (2016) 411–420.
- [52] L. Han, X. Hu, N. A. Adams, Scale separation for multi-scale modeling of free-surface and two-phase flows with the conservative sharp interface method, *Journal of Computational Physics* 280 (2015) 387–403.
- [53] M. Sussman, E. Fatemi, P. Smereka, S. Osher, An improved level set method for incompressible two-phase flows, *Computers & Fluids* 27 (5-6) (1998) 663–680.
- [54] X. Y. Hu, B. Khoo, N. A. Adams, F. Huang, A conservative interface method for compressible flows, *Journal of Computational Physics* 219 (2) (2006) 553–578.